JACS
JOURNAL OF THE AMERICAN CHEMICAL SOCIETY

ARTICLE

pubs.acs.org/JACS

Quantitative Nanoorganized Structural Evolution for a High Efficiency Bulk Heterojunction Polymer Solar Cell

Hsueh-Chung Liao,[†] Cheng-Si Tsao,[*,‡] Tsung-Han Lin,[†] Chih-Min Chuang,[‡] Charn-Ying Chen,[‡] U-Ser Jeng,[§] Chiu-Hun Su,[§] Yang-Fang Chen,[⊥] and Wei-Fang Su[*,†]

[†]Department of Materials Science and Engineering, National Taiwan University, Taipei 106-17, Taiwan

[‡]Institute of Nuclear Energy Research, Longtan, Taoyuan 325-46, Taiwan

[§]National Synchrotron Radiation Research Center, Hsinchu 300-77, Taiwan

[⊥]Department of Physics, National Taiwan University, Taipei 106-17, Taiwan

Supporting Information

ABSTRACT: We have developed an improved small-angle X-ray scattering (SAXS) model and analysis methodology to quantitatively evaluate the nanostructures of a blend system. This method has been applied to resolve the various structures of self-organized poly(3-hexylthiophene) /C61-butyric acid methyl ester (P3HT/PCBM) thin active layer in a solar cell from the studies of both grazing-incidence small-angle X-ray scattering (GISAXS) and grazing-incidence X-ray diffraction (GIXRD). Tuning the various length scales of PCBM-related structures by a different annealing process can provide a flexible approach and better understanding to enhance the power conversion of the P3HT/PCBM solar cell. The quantitative structural characterization by this method includes (1) the mean size, volume fraction, and size distribution of aggregated PCBM clusters, (2) the specific interface area between PCBM and P3HT, (3) the local cluster agglomeration, and (4) the correlation length of the PCBM molecular network within the P3HT phase. The above terms are correlated well with the device performance. The various structural evolutions and transformations (growth and dissolution) between PCBM and P3HT with the variation of annealing history are demonstrated here. This work established a useful SAXS approach to present insight into the modeling of the morphology of P3HT/PCBM film. In situ GISAXS measurements were also conducted to provide informative details of thermal behavior and temporal evolution of PCBM-related structures during phase separation. The results of this investigation significantly extend the current knowledge of the relationship of bulk heterojunction morphology to device performance.

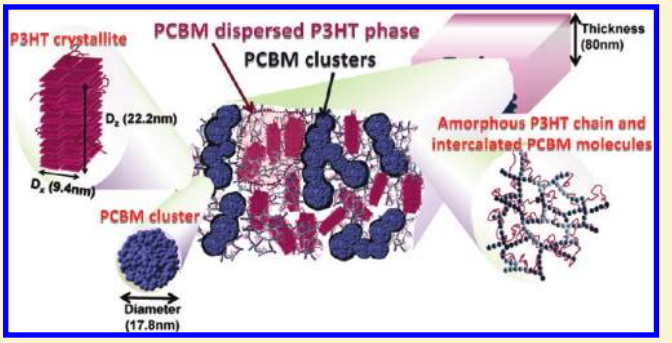

INTRODUCTION

The bulk heterojunction (BHJ) polymer solar cell has attracted a great deal of attention over the past decade. The well-known poly(3-hexylthiophene)/[6,6]-phenyl-C61-butyric acid methyl ester (P3HT/PCBM) BHJ solar cells demonstrated power conversion efficiency (PCE) up to 5%.[1−4] The improvement in PCE of this system critically depends on the three-dimensional self-organized nanostructure of the active layer (morphology of the BHJ film).[5−7] This nanostructure is formed by the phase separation of the P3HT/PCBM blend and is mainly manipulated by thermal or solvent annealing processes.[8−13] The self-organization of P3HT polymer (as donor) into crystallites can enhance the hole mobility/transport and thus improve the PCE. On the other hand, the growth and spatial aggregation of PCBM clusters (as acceptor) formed via the diffusion of PCBM molecules enhance electron transport and also promote device performance. The nanophase-separated domains of P3HT and PCBM in the the BHJ thin film construct an interpenetrating network for the effective transport of charge carriers toward their respective electrodes. However, substantial knowledge of how the practical morphology structure can be tailored to nanoscale by the annealing process is still incomplete.

To date, the detailed structures of three-dimensional BHJ morphology from the local (molecular) scale to the global (approximately tens of nanometers) scale have never been well-understood. The usual tools such as transmission electron microscopy or atomic force microscopy applied for characterizing the morphology of P3HT/PCBM thin films only allow for local observation and have limitations in sampling and sample preparation.[14−18] The microscopic results[19] provide information on the interconnections between nanodomains in bulk heterojunction film. Compared to conventional microscopic tools, the small-angle X-ray scattering (SAXS) technique is a powerful tool to characterize full structures at different scales for a bulk sample.[20−27] The recent small-angle scattering (SAS) studies

Received: April 1, 2011
Published: July 14, 2011

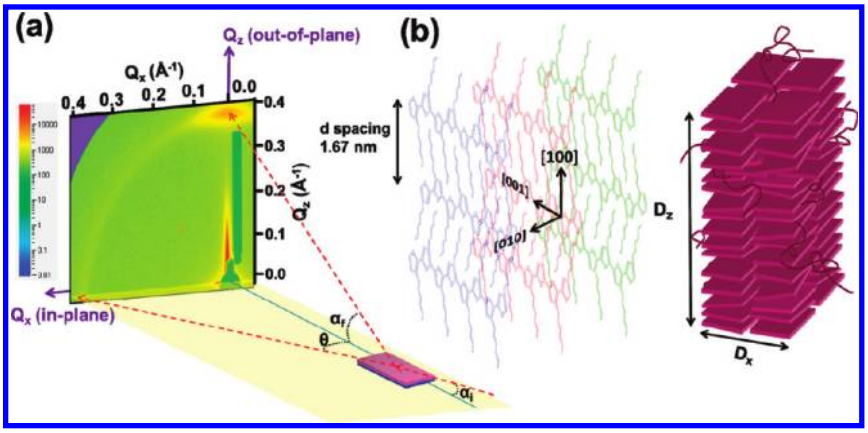

Figure 1. (a) Schematic of GISAXS configuration illustrating the in-plane scattering (Q_X) direction, the out-of-plane scattering (Q^z) direction, and the 2D scattering pattern with α^i, ϑ, and α_f being the incident, in-plane, and out-of-plane scattering angles of X-rays, respectively. (b) The oriented edge-on P3HT crystallite with (100) lamellar structure parallel to the substrate, including unorganized single chain and the crystallographic direction.

on the morphology of P3HT/PCBM films demonstrated the effectiveness of the structure characterization.[20,21] Grazing-incidence X-ray diffraction (GIXRD) has been extensively used to study the characteristics of P3HT crystallites in P3HT/PCBM films. In contrast, the structural characterization of the PCBM phase by using SAXS or grazing-incidence SAXS (GISAXS) is still limited. It was notably pointed out that the variation of PCBM domains would dominate the device performance after the phase-separated structure of P3HT phase becomes stable.[20,21,28−30] A recent small-angle neutron scattering (SANS) study demonstrated that the PCBM nanoparticle plays an important role in the device performance and photoelectric property.[29] Further in-depth GISAXS investigation on the structural evolution of PCBM domains in an annealed thin film are crucial to achieve optimum processing.

To attain optimum processing, we need to improve the SAXS modeling and analysis methodology to study the morphology of the BHJ film. In general, the Guinier approximation of SAXS analysis was usually adopted to determine the size of the PCBM aggregated cluster, assuming monodispersed particles.[20] The recent study by Kiel's group accurately and thoroughly modeled the SANS data by considering the realistic details of practical PCBM clusters in a thin film.[29] Their model assumed that polydispersed PCBM clusters have a Schultz size distribution and have hard-sphere interactions between spherical particles.[31] By model fitting, more important structural parameters were extracted to provide reasonable interpretation of the various photoelectric performances. The present study extends this useful model by linearly adding a Debye−Anderson−Brumberger (DAB) model,[32] which describes an additional larger-scale network structure in the P3HT/PCBM thin film. The results demonstrate that this large structure evolves with the PCBM cluster and is related to the device performance. Moreover, this work used the quantity of specific interface area for effectively evaluating the complex structure of the interpenetrating network comprising the phase-separated PCBM and P3HT domains. This parameter is related to the effect of charge dissociation. It can be model-independent (determined directly by experimental results), obtained from the application of Porod's law.[22] The analysis approach established here can give insight into the full spectrum of structures at different length scales, which are related to the PCE.

The thermal annealing process at 110 °C to 150 °C is the most common way to manipulate the film morphology of the P3HT/PCBM bulk heterojunction solar cell for the improvement of PCE.[9,33−36] Generally, the annealing process investigated is at either preproduction or postproduction stage, which are the thermal treat`ments before and after metal cathode deposition, respectively. The former stage is called preannealing, and the latter stage is called postannealing. Most of the studies only adopted postannealing as the optimum processing. The above annealing treatments are called one-step annealing. Few studies paid attention to the effect of two-step annealing (i.e., combining the annealing treatments at both the pre- and postproduction). The present study demonstrates that the two-step annealing, adopted as an example of feasible annealing designs, can significantly improve the PCE by a factor of 31% compared to conventional postannealing. The PCE values can be correlated to the various nanostructures in the active layer tailored by various annealing treatments, providing useful knowledge to adequately tune the nanomorphology of the thin films. Detailed understanding of the significance of evolution and formation of various phase-separated nanostructures from different thermal treatments can guide the rational processing of BHJ solar cells.

In the present study, we employed the improved GISAXS analysis to thoroughly resolve the self-assembly nanostructure of BHJ films. The combined measurement of GISAXS and GIXRD was used to concurrently study (1) the spatially aggregated structure and molecular dispersion of the PCBM phase and (2) dimensions of P3HT crystallites oriented along the vertical direction of the film. Herein, the P3HT/PCBM (weight ratio = 1:0.8) thin films were thermally treated by designed one-step and two-step annealing processes, respectively. The structural evolution of PCBM-related phases at different length scales with various thermal histories was investigated by GISAXS including (1) the growth, dissolution, and spatial dispersion of PCBM clusters (domains) and (2) structural variation of the large-scale network formed by both P3HT polymer and PCBM molecules. The relationship between the BHJ structure and PCE was discussed with respect to different annealing processes. In situ GISAXS measurement was also performed to reveal the detailed structural evolution and thermal behavior of phase-separated PCBM structures during the heating process and the subsequent annealing stage. The results obtained here are very helpful for designing a potential annealing control and characterizing the morphology of PCBM/P3HT film at different length scales.

■ RESULTS AND DISCUSSION

We have designed several thermal treatments for P3HT/PCBM bulk heterojuction solar cells to correlate between

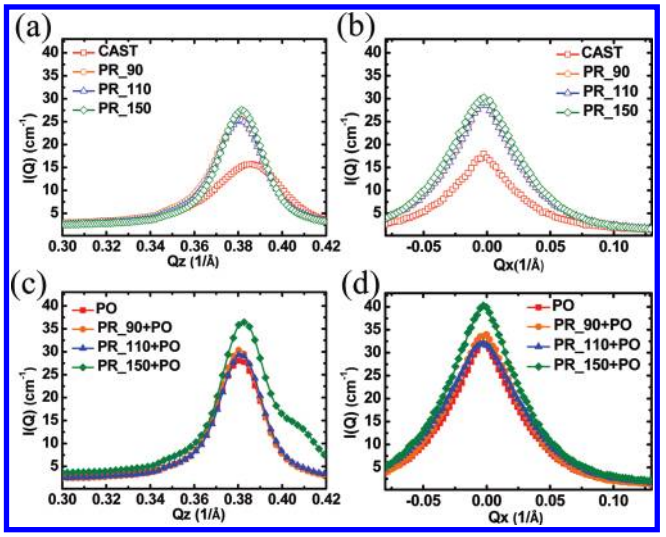

Figure 2. GIXRD profiles reduced along the (a) out-of-plane and (b) in-plane directions of the (100) diffraction spot (around the Q_Z = 0.38 Å^{-1}, Q_X = 0 Å^{-1}) for the P3HT/PCBM thin films without and with various one-step annealing treatments. (c) Out-of-plane and (d) in-plane GIXRD profiles for the P3HT/PCBM thin films with one-step postannealing and various two-step annealing treatments.

structural characteristics of P3HT/PCBM and its corresponding PCEs. The annealing processes used for the solar cell fabrications were identical to the P3HT/PCBM sample films used for X-ray characterization. To define the annealing condition, the P3HT/PCBM films annealed at 90 °C, 110 °C, and 150 °C for 15 min are denoted as PR_90, PR_110, and PR_150, respectively. The film annealed only at 150 °C for 5 min (corresponding to postannealing) is denoted as PO. The above samples were subjected to the so-called one-step annealing. The films annealed at 90 °C, 110 °C, and 150 °C for 15 min (corresponding to preannealing) followed by naturally cooling to room-temperature (RT) for overnight storage and then annealed at 150 °C for 5 min (corresponding to postannealing) are denoted as PR_90+PO, PR_110+PO, and PR_150+PO, respectively. They were subjected to the so-called two-step annealing. The as-cast film without any thermal treatment is denoted as CAST. The difference between the fabricated devices and the corresponding GISAXS samples is the presence of cathode deposition on the film. A recent work[28] demonstrated that the bulk morphologies of P3HT films thermally treated with and without cathode deposition are similar except at the layer interface (~3−5 nm in depth).

We have used a combined synchrotron GIXRD/GISAXS measurement and in situ SAXS measurement to study the morphology of various thermally annealed P3HT/PCBM films (the detailed measurement procedures are described in the Supporting Information). A GIXRD 2D pattern of P3HT/PCBM is displayed in Figure 1a as a function of the scattering vector Q. The GIXRD 2D patterns of P3HT/PCBM thin films with and without annealing treatments are compared (see Supporting Information Figure S1). The weak powder-diffraction ring at $|Q|$ = 0.38 Å^{-1} of the 2D patterns results from the (100) reflection of a few randomly oriented P3HT crystallites (Figure 1). This indicates the presence of P3HT lamellas with spacing of 16.7 Å, which is consistent with the other GIXRD results.[10] For the P3HT layers lying in the (100) plane, the

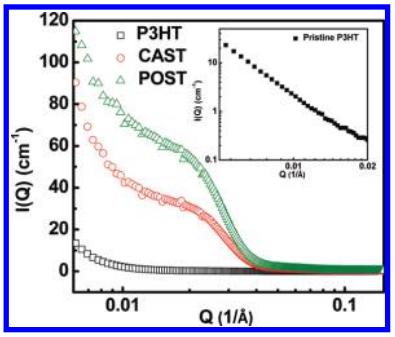

Figure 3. In-plane GISAXS profiles (linear scale) of the pristine P3HT film, the CAST film, and the PO film (annealing once at 150 °C for 5 min). The inset shows the double-log plot of the pristine P3HT film in the low-Q region with the behavior of $I \propto Q^{-4}$.

crystallographic direction [100] (i.e., a axis) is along the alkyl side chain and normal to the P3HT layers. On the other hand, $\pi-\pi$ stacking direction is along the [010] direction (b axis). The backbone chain consisting of the thiophene ring is along the [001] direction (Figure 1b). The high (100) reflection intensity in the z direction, indicated by a spot area, represents the (100) plane of most of the P3HT crystallites oriented along the z direction.[26] This out-of-plane (100) peak indicates that the P3HT lamellas are predominantly oriented parallel to the substrate. The present study focused on the P3HT crystallites of the edge-on type detected by the out-of-plane (100) reflection peak. The other face-on orientation of crystallites (010) is not studied here. The crystal dimensions D_X and D_Z (see Figure 1b) of these P3HT crystallites with the edge-on orientation can be calculated from the widths of the (100) reflection spot ($D_i = 2\pi/\Delta Q$, $i = X$ or Z, where ΔQ is the full width at half-maximum) in the x and z directions, respectively.

The GIXRD profiles reduced along the Q_Z (out-of-plane) and Q_X (in-plane) directions on the spot area for the P3HT/PCBM thin films treated under various annealing conditions are presented in Figure 2. Figure 2a,b shows that the intensities of the diffraction peaks in both directions largely increase after one-step annealing, signifying the increase of crystallinity of the P3HT phase. The enhanced intensity demonstrates the increase in the number of organized P3HT crystallites. The crystal dimensions D_X and D_Z of the P3HT crystallites in the CAST film (without annealing) determined from the GIXRD profiles in the Q_X and Q_Z directions are 10.3 and 12.9 nm, respectively. The values of D_Z of the P3HT crystallites in the thin films annealed at 90 °C to 150 °C for 15 min are almost the same (~21 nm), which is almost insensitive to the effect of annealing temperatures. Similarly, their corresponding D_X values are close to 9.5 nm. The observed effect of annealing temperature (90 °C to 150 °C) on the crystal dimensions is in agreement with the other GIXRD studies[33−36] (i.e., the crystal dimension D_Z for the thin film with one-step annealing is substantially larger than that of the CAST film while their corresponding D_X is regarded as the same as that of the CAST film). For the films treated under various two-step annealing, the GIXRD profiles are almost the same as those (D_Z = 22.3 nm, D_X = 9.5 nm) of the PO film as shown in Figure 2c,d. Apparently, the dimensions of the crystallites are also not affected by the annealing history consisting of the annealing temperatures, the annealing time, and the temperature-cycling effect (two-step treatment).

In contrast to the high thermal stability of P3HT crystallites, the growth of PCBM clusters aggregated through the diffusion of

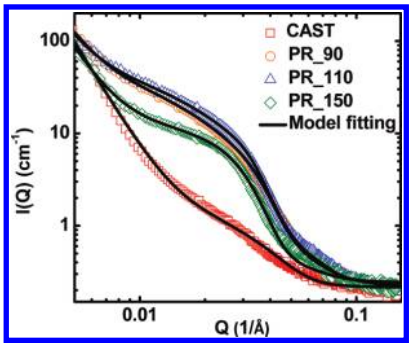

Figure 4. GISAXS profiles of the P3HT/PCBM thin films without annealing and with the one-step annealing treatments at 90 °C, 110 °C, and 150 °C (i.e., the CAST, PR_90, PR_110, and PR_150 films, respectively). The solid lines are calculated by model fitting.

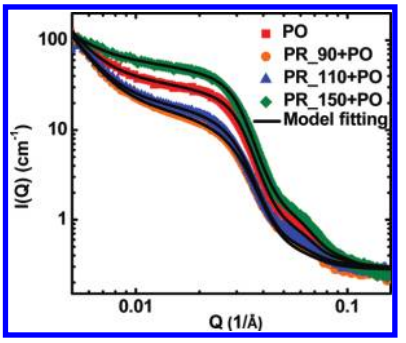

Figure 5. GISAXS profiles of the P3HT/PCBM thin films only with the postannealing (the PO film) and with the two-step annealing treatments preheated at 90 °C, 110 °C, and 150 °C (i.e., the PO, PR_90+PO, PR_110+PO, and PR_150+PO films, respectively). The solid lines are calculated by model fitting.

PCBM molecules out of the P3HT polymer is very sensitive to the corresponding annealing temperatures and two-step treatments (described below). Figure 3 shows the in-plane GISAXS profiles of the pristine P3HT film, the CAST film, and the PO film with the same thickness. Apparently, the main GISAXS intensities can be attributed to the PCBM clusters compared to the flat GISAXS profile of the pristine P3HT film. It was also reported that the GISAXS profiles of the pristine P3HT films with and without annealing treatments are almost the same.[20] This phenomenon agrees with the observation of the other GISAXS study.[20,21,27,28] However, there is a slight upturn of the intensity in the low-Q region (0.005 Å^{-1} to 0.02 Å^{-1}) for the pristine P3HT film, which was rarely mentioned. This upturn demonstrates a power-law scattering behavior $I \propto Q^{-4}$ (see the inset of Figure 3), which is usually observed in the SAS data of polymer system. Additionally, the intensity upturn in the low-Q region for the P3HT/PCBM blend film also demonstrates the similar power-law behavior. This can be attributed to the enhanced scattering contrast due to the PCBM molecules dispersed within the P3HT-rich domains. The SANS study of Kiel's group also pointed out that a significant amount of PCBM molecules exists in the P3HT domains of the annealed blend film. Apparently, relative to the well-known structures of PCBM clusters and P3HT crystallites, there exists a larger scale of structures consisting of (1) the P3HT crystallites, (2) amorphous P3HT region, and (3) the PCBM molecules dispersed or intercalated within P3HT molecular chains. To our knowledge, this study was ignored. Fortunately, it can be characterized by the GISAXS profiles in the low-Q region due to the enhanced X-ray scattering contrast from PCBM molecules inside it. The scattering intensity contributed by such a structure (named herein as PCBM-dispersed P3HT phase) dominates in the low-Q region. Notably, this PCBM-dispersed P3HT phase cannot be regarded as a simple P3HT-rich domain. It is particularly correlated to the network structure of spatial distribution of PCBM molecules intercalated in P3HT molecular chains.[37] The Debye−Anderson−Brumberger equation (DAB model) can be used to describe the scattering of a randomly distributed (nonparticular) two-phase polymer system in terms of correlation length (a measure of the average spacing between phase regions).[23] The present study will demonstrate that the DAB model is a good way to characterize this large scale network of PCBM molecules distributed within the amorphous and around the crystalline P3HT molecular conformations.

Taking into account the accurate SAS model adopted by Kiel's group, the GISAXS profile can be modeled as given by

$$I(Q) = \frac{A}{[1 + (Q\xi)^2]^2} + \eta V(\Delta\rho)^2 \left[\int_0^\infty F_i^2(Q,\sigma_i) f(\sigma_i) d\sigma_i + \int_0^\infty \int_0^\infty F_i(Q,\sigma_i) F_j(Q,\sigma_j) H_{ij}(Q,\sigma_i,\sigma_j) f_i(\sigma_i) f_j(\sigma_j) d\sigma_i d\sigma_j\right] \quad (1)$$

$$F_i(Q,\sigma_i) = 4\pi\left[sin(Q\sigma_i/2) - \frac{1}{2}Q\sigma_i\, cos(Q\sigma_i/2)\right] \quad (2)$$

where the first term on the right-hand side is the DAB model, ξ is the correlation length of the PCBM-dispersed P3HT phase, A is a prefactor treated as an independent fitting parameter and is related to the product of electron density fluctuation, ξ^3, the second term on the right-hand side, is used to model the PCBM clusters, assuming that the polydispersed spheres have Schultz size distribution with hard-sphere interaction between clusters,[31] η is the volume fraction of the PCBM cluster, and $\Delta\rho$ is the difference in scattering length density (SLD) between the PCBM cluster and surrounding matrix. V is the average cluster volume. $F(Q,\sigma_i)^2$ is the form factor of the spherical cluster with a diameter σ_i. $H(Q,\sigma_i,\sigma_j)$ is the pair structure function describing the interaction between clusters with Percus−Yevick approximation. R is the mean cluster radius. The polydispersity, p, is defined as a/R, where a^2 is the variance of the Schultz size distribution $f(\sigma)$. Figure 4 shows the GISAXS profiles of the P3HT/PCBM thin films without annealing and with the one-step annealing treatments at 90 °C, 110 °C, and 150 °C, respectively. Figure 5 shows the GISAXS profiles of the P3HT/PCBM thin films only with the postannealing and with the two-step annealing treatments preheated at 90 °C, 110 °C, and 150 °C, respectively. All profiles can be well-fitted using eq 1, as shown by the solid curves in Figures 4 and 5. The structural parameters, ξ, η, R, and p, determined from the model fitting of eq 1 for the P3HT/PCBM thin films annealed at various conditions, are summarized in Table 1. Basically, the DAB model characterizing the PCBM-dispersed P3HT phase dominates the intensity in the low-Q region. On the other hand, the polydispersed hard-sphere model describing the cluster size and distribution of PCBM domains governs the intensity in intermediate- and high-Q regions. As shown in Figure 6 as an example, the GISAXS intensity for the PO film fitted by a nonlinear least-squares technique[38] over the

Table 1. Structural Parameters Determined by the Porod's Law and Model-Fitting Methods from the P3HT/PCBM Thin Films Treated under Various Annealing Conditions

film	η (%)	R (nm)	P	ξ (nm)	K ($\times 10^{-5}$) (Å^{-4} cm^{-1})	Q_{inv} ($\times 10^{-5}$) (Å^{-3} cm^{-1})	S_v ($\times 10^{-3}$) (Å^{-1})	$S_v/(\eta/R)$
CAST	2.9	4.6	0.31	110	0.37	8.4	3.8	6.0
PR_90	17.0	6.8	0.47	62	0.63	28.4	9.7	3.8
PR_110	19.0	7.4	0.44	65	0.77	33.1	11.3	4.4
PR_150	10.6	7.8	0.26	105	0.46	18.2	7.5	5.5
PO	21.1	8.7	0.29	95	1.03	39.2	13.5	5.7
PR_90+PO	14.1	7.9	0.28	91	0.60	24.7	9.1	5.0
PR_110+PO	15.9	8.3	0.29	85	0.63	28.3	9.4	5.0
PR_150+PO	22.0	8.9	0.29	35	1.22	71.3	9.2	3.7

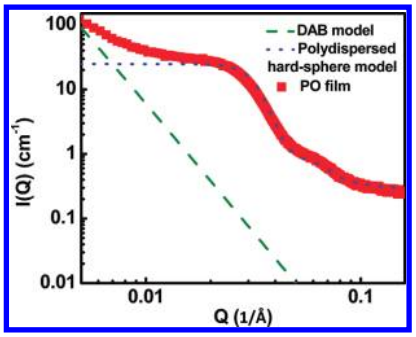

Figure 6. GISAXS intensity calculated by model fitting for the PO film (red square scatter) constituted by the intensities determined by the DAB model (green dashed line) and polydispersed hard-sphere model (blue dotted line).

entire Q region (0.005 Å^{-1} to 0.2 Å^{-1}) can be resolved into two GISAXS intensity profiles calculated by the DAB model and polydispersed hard-sphere model, respectively. Notably, the mean cluster radii (R = 4.6−8.9 nm) of PCBM determined by the model fitting in the present study are in agreement with that (R = 5.9 nm) determined by Kiel's group for P3HT/PCBM annealed at 140 °C. The scattering length density (SLD) contrast, $\Delta\rho$, obtained in the model fitting is discussed in detail in Supporting Information text and Table S1.

As previously mentioned, the PCBM-dispersed P3HT phase can be regarded as the reflection of spatial network structure of PCBM molecules intercalated in the P3HT phase, which is identified by the low-Q GISAXS intensity due to the enhancement of scattering contrast. This network can be roughly characterized by the correlation length ξ of DAB model. This model regards the PCBM-dispersed P3HT phase as a two-phase bicontinuous system comprising (1) P3HT crystallites and (2) the amorphous region of P3HT chains with intercalated PCBM molecules.[37] In Table 1, the correlation length of the CAST blend film (without annealing) is 110 nm, implying that this network of PCBM molecules is distributed throughout the whole thickness of film. After the one-step annealing (for the PR_90 and PR_110), their correlation lengths are largely reduced to be within the length scale of a few P3HT crystallites. This picture reveals that PCBM molecules are located around the P3HT crystallite. This can be attributed to the diffusion of a large amount of PCBM molecules from this dispersed phase into the PCBM clusters. However, the correlation length for the annealing at 150 °C is still unchanged, indicating that a limited amount of PCBM molecules diffused into the clusters. As shown in Table 1, the volume fraction of PCBM clusters in the PR_150 film is half that of the PR_90 and PR_110 films. Although the correlation length and volume fraction are different for various cases, the size of the aggregated PCBM cluster increases with increased annealing temperature from R = 4.6 nm of the CAST film to R = 7.8 nm of the PR_150 film. Basically, for almost all cases, the polydispersity of size distribution decreases with the increase in size of the PCBM clusters. This suggests that some smaller and loose-packed PCBM clusters dissolved and then provided more PCBM molecules, facilitating the growth of larger clusters (like in the Ostwald ripening mechanism[26]) and the reduction in width of size distribution. Note that the phase-separated behavior of PCBM-related phases for one-step annealing at 150 °C is distinctive, which can be attributed to the glass transition and crystallization of the PCBM cluster (described later).

For the P3HT/PCBM film annealed by two-step process, the mean cluster radius in the PR_90+PO and PR_110+PO film grow to be 7.9 and 8.3 nm, respectively, from R = 6.8 and 7.4 nm for the films with the corresponding one-step annealing (the PR_90 and PR_110 films, respectively). However, the volume fractions of PCBM clusters are reduced and the polydisersity of the PCBM cluster size decreased (Table 1). This reveals that some small and loose-packed PCBM clusters dissolved into the PCBM-dispersed P3HT phase during the postannealing step at 150 °C, leading to the reduced volume fraction, deceased polydispersity, and increased correlation length (the network of PCBM molecules). However, the two-step annealing at 150 °C (PR_150+PO) demonstrated a distinctive behavior again, compared to the other two-step annealing treatments. Its correlation length begins to be largely reduced after the additional post-annealing (from ξ = 105 to 35 nm). Moreover, the volume fraction of the PCBM clusters considerably increased compared to the films with only one-step annealing (PR_150). The distinctive result of PR_150+PO can be explained by the thermal behaviors of the pristine PCBM phase. The PCBM has a glass transition temperature (T_g) at around 131 °C[39] and a crystallization temperature (T_c ~149 °C). The incorporation of P3HT into PCBM would lower its T_g and T_c. The thermal treatment (below T_c) may result in the loose-packed PCBM clusters, easily leading to the partial dissolution of the cluster to become PCBM molecules followed by diffusion into the P3HT-rich domain. On the other hand, the PCBM clusters formed at around T_c would compact stacking of the PCBM molecules inside the PCBM cluster, which effectively prevents the clusters from dissolving to become PCBM molecules during the postannealing process. Instead, more PCBM molecules diffused from the PCBM-dispersed P3HT phase into the PCBM cluster, leading to the

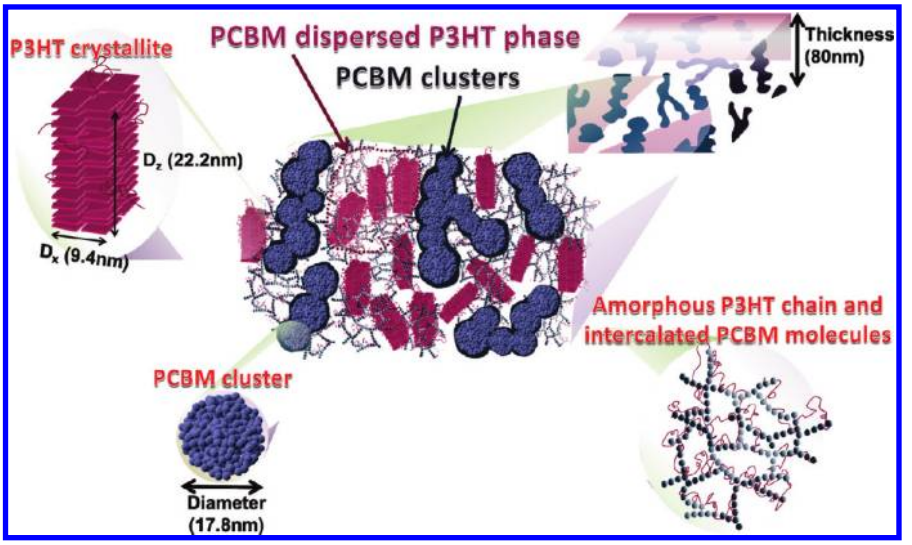

Figure 7. Schematic of the 3D phase-separated structure of a P3HT/PCBM film comprising the PCBM-dispersed P3HT phase (including the P3HT crystallites, the amorphous P3HT chain region, and the network of intercalated PCBM molecules and PCBM clusters shown with different length scales (from upper left to lower left clockwise).

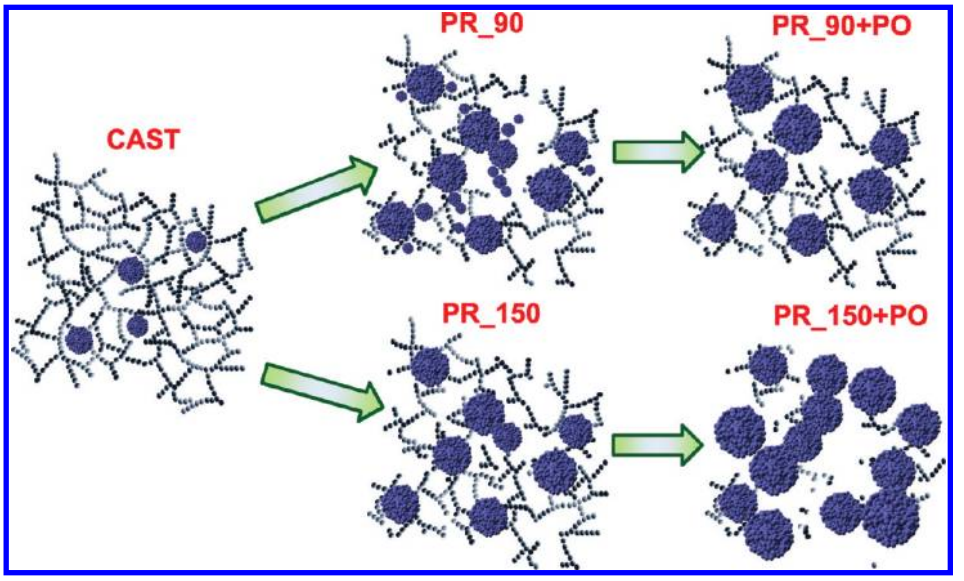

Figure 8. Schematic structural evolution of PCBM clusters and the PCBM molecular network during the first- and second-step annealing process, showing the different behaviors (the growth and dissolution of clusters; the transformation between PCBM clusters and PCBM network) at each step for the films preannealed at 90 °C and 150 °C. The well-separated PCBM clusters (for most of the films) and partial attachment of the PCBM clusters (for PR_150+PO film) are also shown here.

significantly increased volume fraction of PCBM clusters. Moreover, the size of cluster in the PR_150+PO film grows to be 8.9 nm relative to R = 8.1 nm in the PR_150 film. Therefore, the growth of PCBM clusters and the increase of the volume fraction of the PCBM clusters can be manipulated by setting the preannealing temperature at 150 °C and then further heating for the second step. Basically, the change in volume fraction of PCBM clusters is coupled with either the growth or the partial dissolution of the PCBM-dispersed P3HT structure (consistently described by the evolution of correlation length of PCBM molecular network). It can be concluded that except for the growth of clusters like in the Ostwald ripening mechanism, there is a transformation between the PCBM clusters and the PCBM molecular network due to the interdiffusion across the domain interface. The volume fractions of PCBM clusters range from 14% to 22%. It can be estimated that the volume fractions of the corresponding PCBM molecules within the P3HT polymer are from 27% to 19% (the total volume fraction of PCBM phase is ~41%; see Supporting Information, Table S1). It can be speculated that the effect of the P3HT molecular network on the PCE cannot be ignored. According to our results, the 3D self-organized structure of a P3HT/PCBM film (PR_150+PO) comprising the PCBM clusters and PCBM-dispersed P3HT phase (including the P3HT crystallites, the amorphous P3HT chain region, and the network of intercalated PCBM molecules with different length scales) is illustrated in Figure 7. Also shown

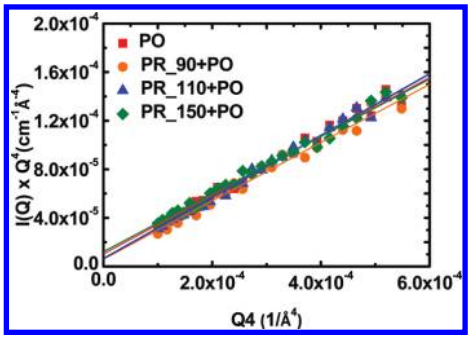

Figure 9. Plot of $Q^4I(Q)$ vs Q^4 corresponding to Figure 5, allowing the determination of K and b values.

in Figure 8 is the structural variation of PCBM during the first- and second-step annealing process (i.e., CAST, PR_90, PR_90 +PO, PR_150, and PR_150+PO for cross-comparison). Note that, on the basis of the fact that the size of P3HT crystallites is not affected by the diffusion of PCBM molecules into or out of the PCBM-dispersed P3HT phase, it can be speculated that most PCBM molecules are mainly located at the amorphous region or around the crystal boundary.

For the PCBM cluster with a sharp polymer−carbon interface, GISAXS manifests an asymptotic behavior in the high-Q region, where $I \propto Q^{-4}$. A model-independent determination of specific interface area S_v (total interface area per unit volume) can be obtained by Porod approximation given in ref 22.

$$K = \lim_{Q \to \infty}[Q^4 \times I(Q)] = 2\pi(\Delta\rho)^2 S_v \quad (3)$$

The constant K is the asymptotic value determined by the product $Q^4I(Q)$ at the high-Q region. The practical application of eq 3 usually involves some uncertainties related to the calibration of absolute measurement and scattering contrast evaluation, etc. To eliminate these uncertainties, the invariant Q_{inv} is used and defined as

$$Q_{inv} = \int_0^\infty Q^2 I(Q)\mathrm{d}Q = 2\pi^2(\Delta\rho)^2\eta(1-\eta) \quad (4)$$

The invariant value Q_{inv} can be obtained from the integration of the GISAXS profile measured. By combining eqs 3 and 4, the specific interface area can be expressed as

$$S_v = \pi\eta(1-\eta)\frac{K}{Q_{inv}} \quad (5)$$

In order to determine the K value, the GISAXS intensity in the high-Q region can be approximated by[40]

$$I(Q) = KQ^{-4} + b \quad (6)$$

The constant value b as background results from the atomic disorder in the surrounding material or thermal motion of polymer molecules. Therefore, the plot of $Q^4I(Q)$ vs Q^4 can be used to determine the values of K (the intercept at $Q = 0$) and b (the slope of straight line fitted) (see Figure 9). Thus, the value of Q_{inv} can be experimentally calculated by the following

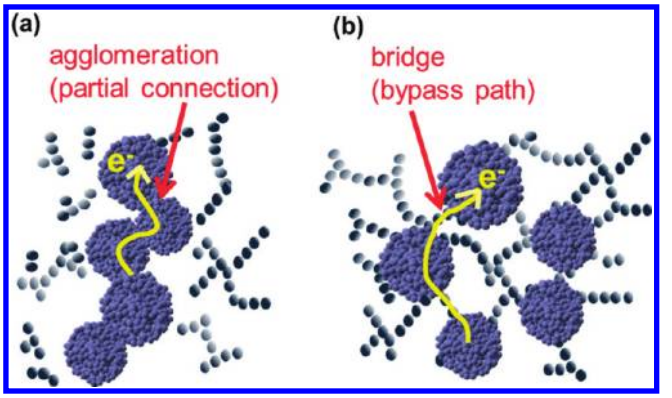

Figure 10. Schematic representation of (a) the partial cluster attachment into the pathway and (b) the bypass path connecting the well-separated PCBM clusters by chain-like or local high-density of PCBM molecules (a bridge between neighboring PCBM clusters).

equation.

$$Q_{inv} = \int_0^{Q\min} I_1(Q)\mathrm{d}Q + \int_{Q\min}^{Q\max}[I(Q) - b]\mathrm{d}Q + \int_{Q\max}^{\infty} I_2(Q)\mathrm{d}Q \quad (7)$$

where Q_{min} and Q_{max} are the lowest- and highest-end Q points obtained. $I_1(Q)$ and $I_2(Q)$ are the functions extrapolated from the two ends of the measured GISAXS profile, respectively. With the known values of η, K, and Q_{inv}, the specific interface area S_v for the films investigated here can be calculated using eq 5 and is listed in Table 1. The value of Q_{inv} monotonically increases with volume fraction η according to eq 4 for $\eta < 0.25$. The model-independently determined values of Q_{inv} (Table 1) can be used to examine the relative order of volume fraction η obtained by model fitting. The result is relatively self-consistent considering the correction of scattering contrast values (see Supporting Information). Upon annealing, the values of S_v (specific interface area) are found to be increased. Actually, many literature reports demonstrated that the measured enhancement of the photoluminescence of annealed P3HT/PCBM film is due to the reduced total interface area.[29,41] Total interface area includes a significant amount of interface area from PCBM molecules within and from P3HT chains. The carriers that dissociate in the discontinuous PCBM molecular network have little opportunity to transport to the electrode. However, it is noteworthy that the S_v proposed here is mainly contributed by the PCBM clusters. Therefore, the S_v cannot be investigated with the photoluminescence spectrum but practically contributes to the photocurrent. Therefore, the largely increased S_v values (resulting from the increased volume fraction of PCBM clusters) can be used to effectively evaluate the improvement of PCE.

To understand how the structure and spatial distribution of PCBM clusters influence the performance of device, the present study proposes four evaluation indices particularly provided by our SAXS results. These indices are as follows: (1) The size of PCBM cluster. The large clusters are beneficial to the mobility of electron in the acceptor phase and to reduce the recombination during the electrons being transported to the electrode. (2) The specific interface area between PCBM and P3HT phases, S_v. It is

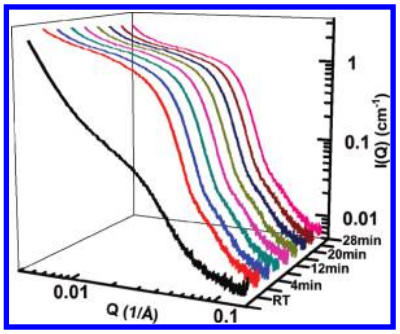

Figure 11. Time-resolved GISAXS profiles of the P3HT/PCBM film annealed at 150 °C together with that of the film at RT.

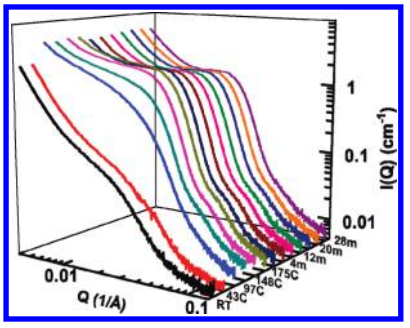

Figure 12. Temperature-dependent GISAXS profiles of the P3HT/PCBM film heated from RT to 180 °C followed by time-resolved GISAXS profiles during the period of annealing.

closely related to the quantity of interface for electron−hole dissociation. The increase of S_v can considerably enhance the photocurrent and thus improve the PCE. (3) The index of quantitatively measuring the agglomeration formed by the partial attachment of some neighboring PCBM clusters into a continuous pathway (see Figure 10a). It is an interesting issue to understand whether the PCBM clusters form such a continuous pathway. However, related knowledge has been limited. The experimental approach for determining this index is established for the first time herein. First of all, the SAXS model-fitting analysis generally assumes that the particles are well-separated. For example, the SANS study of Kiel's group showed a spacing distance between PCBM clusters based on the hard-sphere interaction.[29] Assuming that the PCBM clusters are well-separated, the theoretical specific interface area S_v is proportional to η/R (the value of η/R can be obtained by the model-fitting result of SAXS). On the other hand, for a realistic P3HT/PCBM bulk heterojunction solar cell, the real value of S_v can be measured by the model-independent Porod method based on the two-phase nonparticulate (bicontinuous) system. Therefore, it can be deduced that when the ratio of S_v to η/R is significantly reduced due to a thermal treatment, this implies the transition of structural regimes (i.e, from the regime of well-separated PCBM clusters to that of partially attached PCBM clusters). The partial attachment between PCBM clusters would result in the reduction of actual specific interface area. Table 1 lists the values of S_v-to-η/R ratio for the films with different thermal histories. It is found that the films treated with one-step annealing at 90 °C (PR_90) and 110 °C (PR_110) and two-step annealing preheated at 150 °C (PR_90+PO) have a relatively small value for the ratio of S_v to η/R, revealing the occurrence of highly partial attachment. The films treated under the other conditions have the typical structure of well-separated PCBM clusters and thus have the same order of ratio for S_v to η/R. Figure 8 shows a schematic representation for these structures and their structural transition. (4) The correlation length of the PCBM-dispersed P3HT phase. This correlation length is a characteristic of the spatial distribution or network structure of PCBM molecules intercalated within the amorphous P3HT chains. The local part of the network structure might be regarded as a bridge or bypass path connecting the PCBM clusters which are separated (Figure 10b). The structure with large correlation length may be able to connect several well-separated PCBM clusters that facilitate the transportation of electrons.

The most interesting annealing temperature in this work is 150 °C because it effectively improved the PCE. Particularly, the present study demonstrated that the structural variation at 150 °C has a distinct behavior compared to that of other temperatures that we have mentioned above. Hence, the GISAXS profiles and the analysis results of the films of CAST, PR_150, PO, and PR_150 +PO are chosen to be further compared (see Supporting Information Figure S2; Table 1). The structural evolution shows the turning points with increased annealing time and added postannealing treatment. For example, the GISAXS intensity, volume fraction, and mean radius of PCBM clusters in the film annealed at 150 °C for 15 min (the PR_150 film) remarkably decrease compared to those in the film annealed at 150 °C for 5 min (the PO film). This indicates that PCBM clusters begin to gradually dissolve at annealing times of more than 5 min. However, the GISAXS intensity, volume fraction, and mean radius of PCBM clusters significantly increase in the film annealed at 150 °C for 15 min and then followed by the cooling to RT for overnight and the subsequent postannealing (the PR_150+PO film). This implies that the temperature-cycling effect is able to increase PCBM cluster formation without dissolving the previously generated PCBM clusters in the first stage. The relationship of dissolution behavior of PCBM clusters to the annealing time was not reported elsewhere. To carefully justify this GISAXS observation, we conducted an in situ GISAXS measurement to study the temporal behavior of the evolution of the GISAXS profile for the blend film annealed at 150 °C. As shown in Figure 11, the intensity of the GISAXS profile decreases with increased annealing time, which further confirms the dissolution behavior. Additionally, an in situ GISAXS measurement during both the heating process (from RT up to 180 °C) and the subsequent annealing (at 180 °C) was performed. The similar and more obvious result (see Figure 12) reveals that the GISAXS intensity increases as the temperature is increased but decreases with the annealing time at 180 °C. Basically, both the mean radius and volume fraction of PCBM

Table 2. Device Performance of P3HT/PCBM under Various Annealing Conditions

film	V_{oc} (volt)	J_{sc} (mA/cm^2)	FF (%)	PCE (%)
CAST	0.53	6.1	39	1.2
PR_90	0.51	8.1	39	1.9
PR_110	0.47	9.7	48	2.3
PR_150	0.43	9.6	48	2.0
PO	0.58	9.4	53	2.9
PR_90+PO	0.58	9.8	58	3.3
PR_110+PO	0.60	9.8	57	3.4
PR_150+PO	0.64	10.5	57	3.8

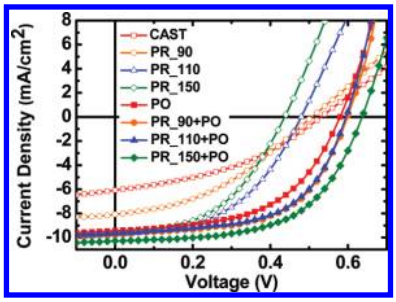

Figure 13. $J-V$ curves of the devices fabricated with the treatments listed in Table 2.

clusters decrease with increasing annealing time while the correlation length of the PCBM-dispersed P3HT phase increases with annealing time. The resultant gain and loss of PCE contributed by them would compensate for each other so that PCE would exhibit uncertain variation with annealing time.

We try to clarify the role of the evaluation indices (mean cluster size, volume fraction of cluster, specific interface area, cluster agglomeration (partial attachment), and correlation length of PCBM network) in correlation to the PCE. Various solar cell devices were fabricated according to the processing of the GISAXS samples. (The detailed processes of device fabrication are described in Supporting Information.) Device performances are summarized in Table 2 for the correlation to the structural parameters listed in Table 1. The corresponding current density−voltage curves are shown in Figure 13. Extensive research has shown that the organization of P3HT significantly affects the hole mobility of the P3HT/PCBM films and thus the device performance. The present study further explores the structural evolution of the PCBM phases and the related effects. The PO film (typical processing) has several features, such as a large mean PCBM cluster, high specific interface area (high cluster volume fraction), and large correlation length (~95 nm), but has well-separated PCBM clusters, exhibiting a PCE of ~2.9%. The PR_110+PO and PR_90+PO devices show a PCE of ~3.3% that can be attributed to the slight partial attachment of clusters (slight reduction in the ratio of S_v to η/R compared to that of the PO film). The PR_150+PO device exhibits the highest PCE of 3.8%, which is a 31% improvement compared to that of the PO device. Apart from the similar indices of large mean PCBM cluster, we attribute the considerable enhancement to the existence of partial connection or attachment of PCBM clusters, forming agglomeration for the continuous pathway. Namely, the electron transport of the PO device can be promoted by (1) the increased volume fraction of PCBM clusters and (2) the PCBM molecular network between well-separated PCBM clusters as a bypass bridge while the electrons in the PR_150+PO device can be directly transported via further agglomeration formed by PCBM clusters. The electron mobility measured by space charge limited current (SCLC) method further provides evidence of the improved electron transport (see Supporting Information Figure S3). The electron mobility of CAST, PO, and PR_150+PO are 4.8×10^{-8} $cm^2/V \cdot s$, 1.0×10^{-3} $cm^2/V \cdot s$, and 4.8×10^{-3} $cm^2/V \cdot s$, respectively. Note that the lower V_{oc} in the devices without postannealing results from the interface behavior between P3HT/PCBM films (3 nm to 5 nm in depth) and the Al cathode.[28] In conclusion, the employment of a two-step annealing process can indeed improve the device performance particularly under the PR_150+PO processing conditions.

CONCLUSIONS

In contrast to the relatively stable behavior of P3HT crystallites, the length scale of PCBM-related structures is important for further improvement of the PCE. The structure and spatial distribution formed in each of the various annealing processes is quantitatively investigated in terms of mean cluster size, volume fraction of cluster, specific interface area, cluster agglomeration, and correlation length of the PCBM molecular network. The P3HT lamellar crystallites cannot be distorted by the diffusion of PCBM molecules dispersed in the amorphous P3HT and the PCBM clustering during thermal treatments. The qualitative interpretation of the various structural evolutions (growth and dissolution) or their transformation between PCBM clusters and the PCBM molecular network significantly extends the current knowledge. The spatial evolution of PCBM clusters from the well-separated regime to the partial attachment regime particularly occurs at 150 °C. The present study demonstrates that changing the annealing process has the capability to further tailor the nanostructure of the photoactive layer of the P3HT/PCBM solar cell. The established relationship between structure and annealing control can serve as a guide for the rational design of annealing conditions. The roles of these structural characteristics in improving the PCE are identified here. The structural parameters and indices can be quantitatively evaluated and well correlated to the PCE.

ASSOCIATED CONTENT

Supporting Information. Experimental section. GIXRD 2D patterns of P3HT/PCBM films with and without thermal annealing. Comparison of the GISAXS profile between CAST, PR_150, POST, and PR_150+POST. Electron mobility measurement of CAST, POST, and PR_150+POST. This material is available free of charge via the Internet at http://pubs.acs.org.

AUTHOR INFORMATION

Corresponding Author
suwf@ntu.edu.tw; cstsao@iner.gov.tw

ACKNOWLEDGMENT

Financial support obtained from National Science Council of Taiwan (99-2120-M-002-011 and 98-3114-E-002-001) and Institute of Nuclear Energy Research (Projects 1002001INER048) is highly appreciated.

REFERENCES

(1) Li, G.; Shrotriya, V.; Huang, J.; Yao, Y.; Moriarty, T.; Emery, K.; Yang, Y. *Nat. Mater.* **2005**, *4*, 864–868.
(2) Ma, W.; Yang, C.; Gong, X.; Lee, K.; Heeger, A. J. *Adv. Funct. Mater.* **2005**, *15*, 1617–1622.
(3) Kim, Y.; Cook, S.; Tuladhar, S. M.; Choulis, S. A.; Nelson, J.; Durrant, J. R.; Bradley, D. D. C.; Giles, M.; Mcculloch, I.; Ha, C.; Ree, M. *Solar Cells. Nat. Mater.* **2005**, *5*, 197–203.
(4) Wu, J. L.; Chen, F. C.; Hsiao, Y. S.; Chien, F. C.; Chen, P.; Kuo, C. H.; Huang, M. H.; Hsu, C. S. *ACS Nano* **2011**, *5*, 959–967.
(5) Andersson, V.; Herland, A.; Masich, S.; Inganäs, O. *Nano Lett.* **2009**, *9*, 853–855.
(6) Bavel, S. S. V.; Sourty, E.; With, G. D.; Loos, J. *Nano Lett.* **2009**, *9*, 507–513.

(7) Yu, B. Y.; Lin, W. C.; Wang, W. B.; Iida, S. I.; Chen, S. Z.; Liu, C. Y.; Kuo, C. H.; Lee, S. H.; Kao, W. L.; Yen, G. J.; You, W. W.; Liu, C. P.; Jou, J. H.; Shyue, J. J. *ACS Nano* **2010**, *4*, 833–840.
(8) Mihailetchi, V. D.; Xie, H.; Boer, B. D.; Koster, L. J. A.; Blom, P. W. M. *Adv. Funct. Mater.* **2006**, *16*, 699–708.
(9) Nguyen, L. H.; Hoppe, H.; Erb, T.; Günes, S.; Gobsch, G.; Sariciftci, N. S. *Adv. Funct. Mater.* **2007**, *17*, 1071–1078.
(10) Verploegen, E.; Mondal, R.; Bettinger, C. J.; Sok, S.; Toney, M. F.; Bao, Z. *Adv. Funct. Mater.* **2010**, *20*, 3519–3529.
(11) Li, G.; Yao, Y.; Yang, H.; Shrotriya, V.; Yang, G.; Yang, Y. *Adv. Funct. Mater.* **2007**, *17*, 1636–1644.
(12) Miller, S.; Fanchini, G.; Lin, Y. Y.; Li, C.; Chen, C. W.; Su, W. F. *J. Mater. Chem.* **2008**, *18*, 306–312.
(13) Bull, T. A.; Pingree, L. S. C.; Jenekhe, S. A.; Ginger, D. S.; Luscombe, C. K. *ACS Nano* **2009**, *3*, 627–636.
(14) Howard, I. A.; Mauer, R.; Meister, M.; Laquai, F. *J. Am. Chem. Soc.* **2010**, *132*, 14866–14876.
(15) Giridharagopal, R.; Ginger, D. S. *J. Phys. Chem. Lett.* **2010**, *1*, 1160–1169.
(16) Guo, J.; Ohkita, H; Benten, H.; Ito, H. *J. Am. Chem. Soc.* **2010**, *132*, 6154–6164.
(17) Hamadani, B. H.; Jung, S.; Haney, P. M.; Richter, L. J.; Zhitenev, N. B. *Nano Lett.* **2010**, *10*, 1611–1617.
(18) Gao, Y.; Grey, J. K. *J. Am. Chem. Soc.* **2009**, *131*, 9654–9662.
(19) Sourty, E.; Bavel, S. V.; Lu, K.; Guerra, R.; Bar, G.; Loos, J. *Microsc. Microanal.* **2009**, *15*, 251–258.
(20) Chiu, M. Y.; Jeng, U. S.; Su, C. H.; Liang, K. S.; Wei, K. H. *Adv. Mater.* **2008**, *20*, 2573–2578.
(21) Chiu, M. Y.; Jeng, U. S.; Su, M. S.; Wei, K. H. *Macromolecules* **2010**, *43*, 428–432.
(22) Glatter, O.; Kratky, O. *Small-Angle X-Ray Scattering*; Academic Press: London, 1982.
(23) Lin, T. L.; Jeng, U. S.; Tsao, C. S.; Liu, W. J.; Canteewala, T.; Chiang, L. Y. *J. Phys. Chem. B* **2004**, *108*, 14884–14888.
(24) Tsao, C. S.; Li, M.; Zhang, Y.; Leao, J. B.; Chiang, W. S.; Chung, T. Y.; Tzeng, Y. R.; Yu, M. S.; Chen, S. H. *J. Phys. Chem. C* **2010**, *114*, 19895–19900.
(25) Li, Y. C.; Chen, K. B.; Chen, H. L.; Hsu, C. S.; Tsao, C. S.; Chen, J. H.; Chen, S. A. *Langmuir* **2006**, *22*, 11009–11015.
(26) Tsao, C. S.; Chen, C. Y.; Cheng, U. S.; Kuo, T. Y. *Acta Mater.* **2006**, *54*, 4621–4631.
(27) Tsao, C. S.; Yu, M. S.; Chung, T. Y.; Wu, H. C.; Wang, C. Y.; Chang, K. S.; Chen, H. L. *J. Am. Chem. Soc.* **2007**, *129*, 15997–16004.
(28) Chen, D.; Nakahara, A.; Wei, D.; Nordlund, D.; Russell, T. P. *Nano Lett.* **2011**, *2*, 561–567.
(29) Kiel, J. W.; Eberle, A. P. R.; Mackay, M. E. *Phys. Rev. Lett.* **2010**, *105*, 167801−1–167801−4.
(30) Shin, M.; Kim, H.; Park, J.; Nam, S.; Heo, K.; Ree, M.; Ha, C. S.; Kim, Y. *Adv. Funct. Mater.* **2010**, *20*, 748–754.
(31) Griffith, W. L.; Triolo, R.; Compere, A. L. *Phys. Rev. A* **1987**, *35*, 2200.
(32) Debye, P.; Anderson, R.; Brumberger, H. *J. Appl. Phys.* **1957**, *28*, 679.
(33) Kim, Y.; Choulis, S. A.; Nelson, J.; Bradley, D. D. C.; Cook, S.; Durrant, J. R. *J. Mater. Sci.* **2005**, *40*, 1371–1376.
(34) Hiorns, R. C.; Bettignies, R. D.; Leroy, J.; Bailly, S.; Firon, M.; Sentein, C.; Khoukh, A.; Preud'homme, H.; Dagron-Lartigau, C. *Adv. Funct. Mater.* **2006**, *16*, 2263–2273.
(35) Watts, B.; Belcher, W. J.; Thomsen, L.; Ade, H.; Dastoor, P. C. *Macromolecules* **2009**, *42*, 8392–8397.
(36) Huang, Y. C.; Liao, Y. C.; Li, S. S.; Wu, M. C.; Chen, C. W.; Su, W. F. *Sol. Energy Mater. Sol. Cells* **2009**, *93*, 888–892.
(37) Cates, N. C.; Gysel, R.; Beiley, Z.; Miller, C. E.; Toney, M. F.; Heeney, M.; McCulloh, I.; McGehee, M. D. *Nano Lett.* **2009**, *9*, 4153–4157.
(38) Kline, S. R. *J. Appl. Crystallogr.* **2006**, *39*, 895–900.
(39) Zhao, J.; Swinnen, N.; Assche, G. V.; Manca, J.; Vanderzande, D.; Mele, B. V. *J. Phys. Chem. B* **2009**, *113*, 1587–1591.
(40) Laudisio, G.; Dash, R. K.; Singer, J. P.; Yushin, G.; Gogotsi, Y.; Fischer, J. E. *Langmuir* **2006**, *22*, 8945–8950.
(41) Mihailetchi, V. D.; Xie, H.; Boer, B. D.; Koster, L. J. A.; Blom, P. W. M. *Adv. Funct. Mater.* **2006**, *16*, 699–708.